

# Strong Kinetic-Inductance Kerr Nonlinearity with Titanium Nitride Nanowires

Chaitali Joshi,<sup>1,2</sup> Wenyuan Chen,<sup>1</sup> Henry G. LeDuc,<sup>3</sup> Peter K. Day,<sup>3</sup> and Mohammad Mirhosseini<sup>1,2,\*</sup>

<sup>1</sup> Moore Laboratories of Electrical Engineering, California Institute of Technology, Pasadena, California, USA

<sup>2</sup> Institute of Quantum Information and Matter, California Institute of Technology, Pasadena, California, USA

<sup>3</sup> Jet Propulsion Laboratory, Pasadena, California, USA



(Received 30 July 2022; accepted 9 November 2022; published 28 December 2022)

Thin films of disordered superconductors such as titanium nitride (TiN) exhibit large kinetic inductance (KI), high critical temperature, and large quality factors at the single-photon level. KI nonlinearity can be exploited as an alternative to Josephson junctions to create novel nonlinear quantum devices with the potential to operate at higher frequencies and at elevated temperatures. We study a means of magnifying KI nonlinearity by confining the current density of resonant electromagnetic modes in nanowires with a small volume  $V \simeq 10^{-4} \mu\text{m}^3$ . Using this concept, we realize microwave-frequency Kerr cavities with a maximum Kerr shift per photon of  $K/2\pi = 123.5 \pm 12 \text{ kHz}$  and report a nonlinearity-to-linewidth ratio  $K/\gamma = 21\%$ . With improved design, our devices are expected to approach the regime of strong quantum nonlinearity in the millimeter-wave spectrum.

DOI: 10.1103/PhysRevApplied.18.064088

## I. INTRODUCTION

Circuit quantum electrodynamic systems rely on superconducting qubits based on Josephson junctions. The inductance of a Josephson junction is a nonlinear function of the current tunneling through it, which formally behaves as a Kerr nonlinearity and gives rise to discrete energy levels in a qubit. Alternatively, a current-dependent inductance can be realized via the kinetic energy of current-carrying cooper pairs in a superconducting wire. This source of nonlinear electromagnetic response is currently being explored for parametric quantum frequency conversion and amplification in the millimeter-wave band (100–300 GHz), and at elevated temperatures (above 1 K) [1,2], where using (Al-based) Josephson junctions is not feasible.

While parametric operations are possible with weak nonlinearities, an interesting possibility is to create a strongly nonlinear response where the induced self-Kerr shift per photon in a resonator is comparable to its intrinsic linewidth. Resonators in this regime can be used for synthesizing quantum states of radiation [3]. Ultimately, when the nonlinearity exceeds the dissipation rate in a resonator the system effectively behaves as qubit [4,5]. This concept was recently materialized in transmon qubits based on kinetic inductance (KI) in oxidized (granular) aluminum films (GrAl) [6–9]. However, the relatively low critical temperature of GrAl (2–3 K) makes it unsuitable

for application in the millimeter-wave band or at elevated temperatures.

Thin films of disordered superconductors such as titanium nitride (TiN), niobium titanium nitride (NbTiN), and niobium nitride (NbN) provide an alternative choice of materials. These films exhibit large KI, and high critical temperature (up to 14.5 K for NbTiN) [10], making them suitable candidates for developing quantum circuits operating at increased temperatures and frequencies while circumventing dissipation due to quasiparticle generation. Additionally, resonators fabricated from these materials can achieve large intrinsic quality factors factors ( $10^5$ – $10^7$  in the single-photon regime [11–14]), and have been widely utilized for high-impedance quantum circuits, amplifiers, and detectors [15–23]. Microwave resonators fabricated from disordered superconductors are also known to be resilient to in-plane magnetic fields with  $Q$ -factors of  $10^5$  when operated in magnetic fields up to a few teslas [19,24,25]. This makes them suitable for hybrid quantum systems such as superconducting resonators coupled to spin qubits which require large magnetic fields for operation. The nonlinearity of KI films can also be used to develop microwave resonators with tunable frequencies using external magnetic fields of a few milliteslas [26,27]. Despite these attractive properties, the KI nonlinearity in nitride films tends to be weaker than in GrAl. This is, in part, due to the distinct underlying sources of KI in homogeneously disordered [28,29] and granular materials [8,30], where in the latter the insulating oxide barriers in the microstructure of the film act as weak Josephson links.

\*Corresponding author.  
<http://qubit.caltech.edu>

In this work, we amplify the KI nonlinearity by engineering the geometry of planar resonators fabricated from TiN. Our design maximizes the nonlinear response by confining the current density of the resonator mode in nanowires with a small lateral width (between about 20 and 200 nm) patterned on a thin film (14 nm thick). Further, we maximize the magnitude of current quantum zero-point fluctuations by minimizing the resonator impedance, which is achieved by employing narrow-gap planar capacitors. Using these strategies, we achieve self-Kerr nonlinearity rates in the range of 2–120 kHz in nanowire resonators with intrinsic quality factors reaching  $3.5 \times 10^4$  in the best devices. The maximum measured single-photon Kerr-shift-to-linewidth ratio in our experiment reaches  $0.21 \pm 0.02$ , which significantly exceeds the nonlinearities reported in prior work with homogeneously

disordered superconductors [20]. These results motivate future work in optimizing device design, where quantum nonlinearities are expected to be within reach at higher frequencies.

## II. DEVICE DESIGN

Our design concept is to realize an electromagnetic resonant mode with the magnetic energy density confined to a small volume with a large current density. This can be achieved in a compact microwave resonator, where a nanowire with a large KI connects the two pads of a planar rectangular capacitor [see Fig. 1(a)]. For weak currents, the KI of the nanowire can be modeled as a quadratic function  $L_w/L_0 = 1 + (I/I_*)^2$ , where  $I_*$  is the nonlinear scaling current set by material properties and wire cross section

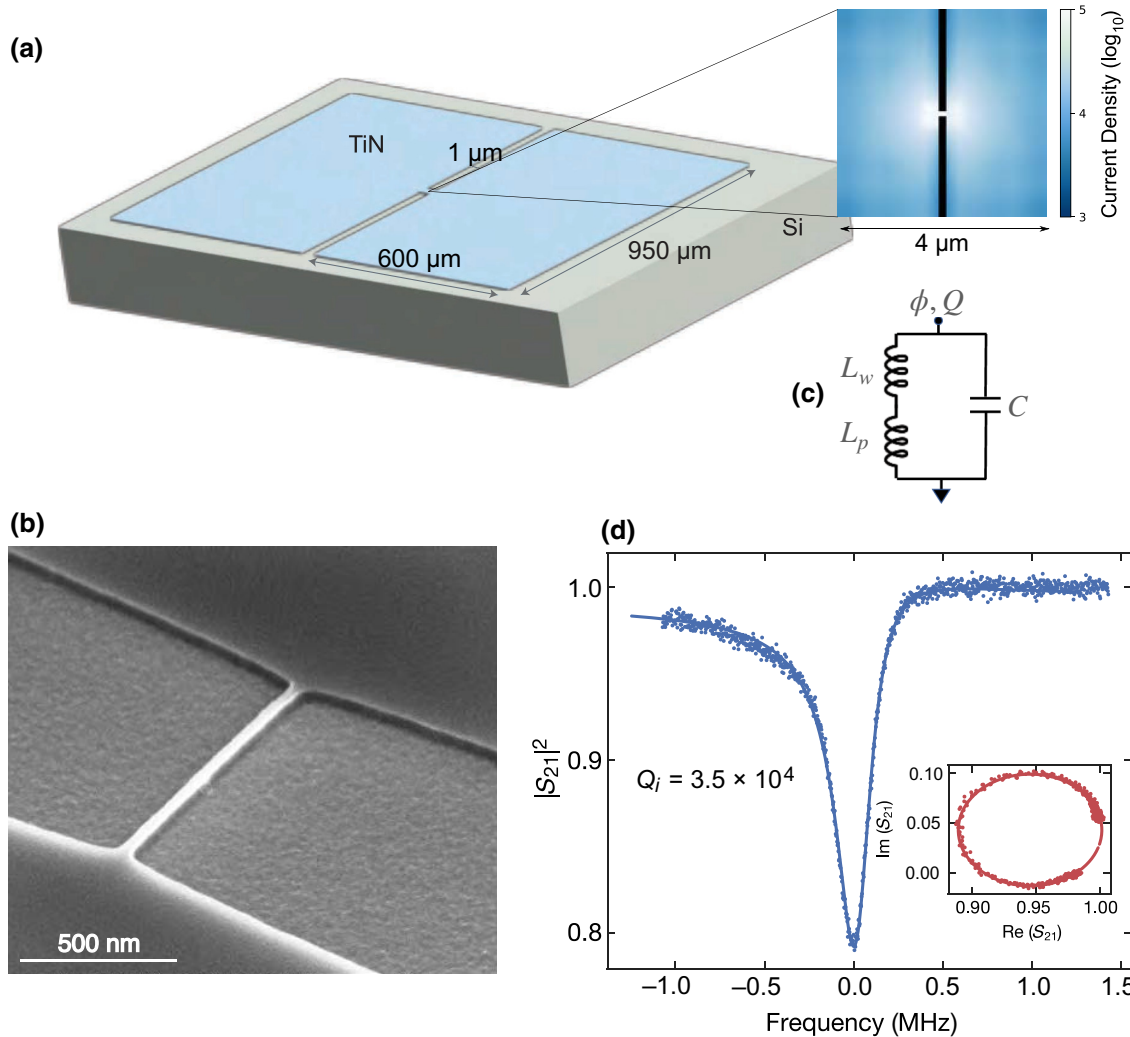


FIG. 1. Nanowire resonator design. (a) The resonator consists of a miniature nanowire with a width of 20–40 nm, shunted by coplanar capacitor pads fabricated from thin film TiN. Inset: Simulated current density in the nanowire region. The current density is maximum in the nanowire and drops in the capacitor pad region in the immediate vicinity of the wire. The nanowire geometry enhances zero-point fluctuations, maximizing the Kerr shift per photon. (b) Scanning electron microscope image of a fabricated nanowire with width  $w = 38$  nm. (c) Circuit model of the nanowire resonator. (d) Typical linear response of a nanowire resonator (see Table I).

[10,31,32]. The Hamiltonian of this *LC*-resonator can be written as

$$H = \frac{Q^2}{2C} + \frac{\phi^2}{2L} + \frac{1}{4} \frac{\phi^4}{I_*^2} \frac{L_w}{L^4}. \quad (1)$$

Here,  $Q$  and  $\phi$  are the charge and flux node variables, and  $C$  is the total capacitance. The parameter  $L$  is the total inductance of the resonator, which includes the KI of the nanowire ( $L_w$ ) as well as the contribution from the nonzero current distribution in the capacitor pads ( $L_p$ ). The first two terms in the Hamiltonian describe a harmonic oscillator with frequency  $\omega = 1/\sqrt{LC}$  and the last term models the nonlinear behavior due to the current-dependent KI in the nanowire. Applying circuit quantization [33], Eq. (1) can be rewritten in terms of the creation ( $\hat{a}^\dagger$ ) and annihilation ( $\hat{a}$ ) operators of the *LC* circuit. The nonlinear term in the Hamiltonian can be simplified by expanding the quadratic current term as  $\hat{I}^4 = I_{ZPF}^4 (\hat{a} + \hat{a}^\dagger)^4$ , where  $I_{ZPF} = \sqrt{\hbar\omega/2L}$  is the current zero-point fluctuation. Retaining only the photon-number-conserving terms, we find

$$\hat{H} = \hbar(\omega - K) \left( \hat{a}^\dagger \hat{a} + \frac{1}{2} \right) - \frac{K}{2} \hat{a}^\dagger \hat{a}^\dagger \hat{a} \hat{a},$$

with the Kerr-shift per photon  $K$  defined as

$$K = \frac{3}{2} \frac{\omega L_w}{\omega L} \left( \frac{I_{ZPF}}{I_*} \right)^2. \quad (2)$$

As evident in Eq. (2), a unity Kerr-shift-to-linewidth ratio ( $K/\gamma \approx 1$ ) can be achieved if the zero-point fluctuations of the current are enhanced sufficiently to reach  $(I_{ZPF}/I_*)^2 \approx 1/Q$ , where  $Q = \omega/\gamma$  is the quality factor of the resonator. We pursue this goal by minimizing the total device inductance to achieve a large  $I_{ZPF}$  while maintaining a sufficiently large wire participation ratio  $L_w/L$ .

The expression for the Kerr coefficient can be further simplified by substituting the scaling current as a function of material properties [10],

$$I_* = J_* w t = \sqrt{\frac{\pi N_0 \Delta_0^3}{\hbar \rho_n}} w t, \quad (3)$$

where  $N_0$  is the density of electron states at the Fermi energy and  $\Delta_0 \approx 1.76 k_B T_c$  is the energy gap at zero temperature. The parameter  $\rho_n$  denotes the normal-state resistivity of the film,  $w$  is the wire width, and  $t$  is the film thickness. Similarly, the KI of the nanowire can be expressed as a function of geometry and material properties  $L_w = \hbar(\rho_n/\pi \Delta_0)(l/wt)$ , where  $l$  is the wire length. Finally, defining the participation ratio of KI in the wire to the total

inductance as  $\alpha = L_w/L$ , Eq. (2) can be rewritten as

$$K = \frac{3}{4} \frac{\hbar \omega^2}{N_0 \Delta_0^2} \frac{\alpha^2}{V}, \quad (4)$$

where  $V = wlt$  is the volume of the nanowire.

In terms of the material properties, an important observation is that the Kerr coefficient is independent of the film resistivity (so far the nanowire's KI dominates all sources of parasitic inductance). Additionally, the inverse scaling with the energy gap  $\Delta_0$  motivates our choice of TiN over niobium-based nitride films, which in general have higher critical temperatures. The geometrical scaling is by and large set by the parameter  $V$ , which favors nanowires with the minimum possible dimensions. However, in the presence of a nonzero pad inductance  $L_p$ , reducing the wire length beyond a certain point reduces the Kerr coefficient via the participation ratio  $\alpha$ . Considering this trade-off, choosing optimum dimension parameters requires the knowledge of film resistivity and the feasible fabrication geometries for nanowires. In our experiment, we realize  $L_w$  between 800 pH and 1.6 nH, requiring a shunt capacitance of the order of 0.3 pF to achieve resonance frequencies in our measurement band (6–8.5 GHz).

Realizing a capacitance of this magnitude with planar geometries is challenging. A large capacitor footprint translates to increased radiation loss and the formation of parasitic self-resonances. Alternatively, choosing narrow gaps and long aspect ratios in interdigitated geometries results in additional loss from surface two-level defects and a reduced participation ratio due to increased pad inductance  $L_p$ . Using finite-element method (FEM) modeling as a guide to bound these effects, we have chosen a symmetric rectangular capacitor geometry with a total pad area of 1.14 mm<sup>2</sup> and a narrow gap of 1 μm [see Fig. 1(a)]. As detailed in the following sections, we perform experiments on fabricated devices to evaluate the range of quality factors within reach for this extreme geometry.

### III. FILM CHARACTERIZATION

Our goal of maximizing nonlinearity motivates using films with minimum possible thicknesses. However, reducing the film thickness results in increasing disorder, which eventually induces a superconducting-to-insulating transition [11,34]. As a result, the choice of film thickness requires balancing the competing requirements for achieving a large KI, a large critical temperature, and a low intrinsic loss tangent. Considering these factors and previous results in the literature [11], we chose to work with films in the 10–20 nm thickness range. The TiN samples used in our experiment were deposited using reactive sputtering on a high-resistivity ( $\rho > 10$  kΩ) Si substrate and measured with an ellipsometer to have a thickness of 14 nm.

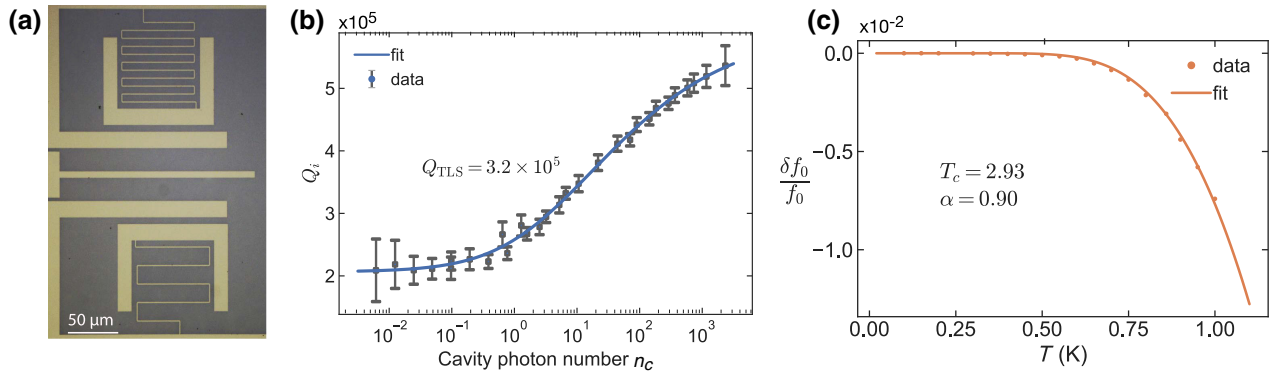


FIG. 2. Film characterization. (a) Optical image of two compact, quarter-wave test resonators. The resonator consists of a meandered wire shunted by a C-shaped capacitor pad. (b) Measured intrinsic quality factor of the compact resonators as a function of mean cavity photon number  $n_c$ , showing characteristic behavior of two-level-systems (TLS) loss. The power-dependent quality factor  $Q_{\text{TLS}}$  is  $3.2 \times 10^5$ . At powers exceeding  $n_c = 3 \times 10^3$ , the resonator response becomes nonlinear. (c) Measurement of critical temperature  $T_c$  using temperature-dependent resonant-frequency shift. Fits to data are from numerical integration of surface impedance obtained from the Mattis-Bardeen equations.

To extract the film parameters, we fabricate and measure quarter-wave “test” resonators using standard single electron-beam lithography followed by inductively coupled plasma reactive ion etching (ICP-RIE) in SF<sub>6</sub> and Ar [Fig. 2(a)]. We cool samples in a dilution refrigerator with a base temperature of 10 mK and measure coherent reflection from the devices via a circulator using a vector network analyzer (VNA). We extract the resonance frequency and the internal quality factors of the resonators by fitting a Lorentzian lineshape to the measured resonator response [see Fig. 1(c)]. We fit the extracted resonance frequency for resonators with varying wire lengths to FEM simulation results to calculate the film sheet KI ( $L_s = 40 \pm 1$  pH/◻; see Appendix A). Due to the large wire cross sections used in these experiments (0.25–2 μm), the test resonators exhibit weak nonlinearities ( $K/2\pi \approx 5$ –50 Hz), observable nevertheless at high photon numbers. Characterizing the nonlinearity using two-tone spectroscopy (detailed in the next section), we find the nonlinear scaling current density of the film ( $J_* = 3.95 \pm 0.75$  MA/cm<sup>2</sup>).

We characterize the film loss tangent by fitting the change in the internal quality factor of the resonators as a function of the number of photons in the cavity. As evident in Fig. 2(b), the internal  $Q$ -factors show a saturation behavior that is characteristic of TLS loss [12,14]. We perform  $Q$ -factor measurements over a sample size of seven test resonators and find an average (standard deviation) of  $2.1 \times 10^5$  ( $9 \times 10^4$ ) at sub-single-photon powers. The  $Q$ -factors at high photon numbers do not show excessive quasiparticle loss despite the thin-film thickness, and are comparable to reported values in previous work with films deposited via atomic layer deposition [34]. Importantly, we did not observe a statistically significant trend with respect to the wire width of the test resonators.

Finally, we measure the critical temperature of the TiN film by measuring the temperature dependence of the compact resonator frequency [Fig. 2(c)]. The temperature dependence of the surface impedance  $X_s$  results in a change in the resonator frequency, which is given by [35,36]

$$\frac{\delta f_0}{f_0} = -\frac{\alpha}{2} \frac{X_s(T) - X_s(0)}{X_s(0)} \quad (5)$$

where  $\alpha$  is the KI inductance fraction of the resonator (extracted from FEM simulation of the device) and  $\delta f_0$  is the change in the cavity resonance frequency. We use surface impedance calculated from numerical integration of the Mattis-Bardeen equations ([35,37]) to fit the fractional change in resonance frequency  $\delta f_0/f_0$  and extract  $T_c = 2.9$  K.

#### IV. NONLINEAR RESPONSE OF NANOWIRE RESONATORS

Having established our film parameters, we aim to realize nanowire resonators with the smallest feasible dimensions. To achieve this, we have optimized our fabrication procedure and achieved wire widths as small as 20 nm with run-to-run repeatability of about 3–4 nm (see Appendix A). We have measured the nonlinear response of fabricated resonators with varying wire dimensions (Table I). The dimensions of the capacitor pads were chosen to be identical for all resonators, and the wire length was adjusted, for each width, to achieve resonance frequencies in the range of 6–8.5 GHz.

We perform linear spectroscopy and find that the nanowire resonators exhibit the characteristic shape of Duffing oscillators [see Fig. 3(a)], consistent with a Kerr

TABLE I. Summary of results. The uncertainty in calculating the Kerr coefficient is dominated by the uncertainties in the measurement of the frequency-dependent input line attenuation. The internal linewidth  $\gamma$  of all resonators was extracted from the complex amplitude response at single-photon ( $n_c \approx 0.3$ ) drive levels.

	$f_0$ (GHz)	Width (nm)	Length (nm)	Linewidth ( $\gamma$ , kHz)	Intrinsic $Q$ -factors	Kerr shift ( $K/2\pi$ , kHz)	$K/\gamma$ (%)
1	6.30	$18 \pm 2$	460	580	$1.08 \times 10^4$	$123.5 \pm 12$	$21 \pm 2$
2	8.48 <sup>a</sup>	$38 \pm 2$	600	1600	$0.53 \times 10^4$	$88 \pm 11$	$5.5 \pm 0.7$
3	8.07	$38 \pm 2$	800	800	$1 \times 10^4$	$72.5 \pm 9.5$	$9 \pm 1$
4	7.03	$36 \pm 2$	1450	310	$2.3 \times 10^4$	$46 \pm 9$	$15 \pm 3$
5	7.12 <sup>a</sup>	$38 \pm 2$	1200	1000	$0.71 \times 10^4$	$42 \pm 8$	$4.2 \pm 0.8$
6	6.50	$44 \pm 2$	1800	2300	$0.2 \times 10^4$	$15.5 \pm 2.5$	$0.7 \pm 0.1$
7	7.70	$225 \pm 2$	7250	220	$3.5 \times 10^4$	$2.2 \pm 0.3$	$1 \pm 0.15$

<sup>a</sup>These devices were on a separate chip (see text).

nonlinear response. As expected, beyond a critical circulating power in the resonator, the system undergoes bifurcation and exhibits bistability [38]. In addition to the power-dependent frequency shift, we observe an increase in the internal linewidth of the resonator with the increasing number of photons in the cavity. Given the very small photon numbers used in these measurements ( $n_c \sim 1$ –10), the broadening is unlikely to be caused by classical nonlinear loss processes. Instead, we attribute this effect to dephasing caused by quantum fluctuations in the number of interactivity photons (i.e., the photon shot noise). This explanation is further substantiated by observing a linear dependence of the linewidth from the fit to the square root of the intracavity photon number (see Appendix D). Despite the rich underlying physics, which verifies the strong nonlinear response of our system, this photon-number-dependent cavity linewidth makes it challenging to extract the self-Kerr coefficient ( $K$ ) from a direct fit to the Duffing oscillator model.

As an alternative way of finding  $K$ , we perform two-tone spectroscopy. In these measurements, a detuned coherent pump tone is applied to the cavity while measuring the spectral response to a weak resonant probe [see Fig. 3(b)]. The power of the probe tone is set such that the cavity population from the resonant drive remains two orders of magnitude lower than that of the pump tone. Crucially, the large detuning of the pump tone from the cavity in this measurement scheme leads to a much faster fluctuation time scale in the number of intracavity photons, effectively eliminating broadening from photon shot noise [39]. As evident in Fig. 3(b), varying the number of photons from the pump does not lead to any significant change in the resonator linewidth, further verifying the role of photon shot noise.

To fit the data, we calibrate the power delivered to the chip precisely by measuring the frequency-dependent input line attenuation using thermometry of a cryogenic  $50 \Omega$  termination (see Appendix C). From linear fits to the

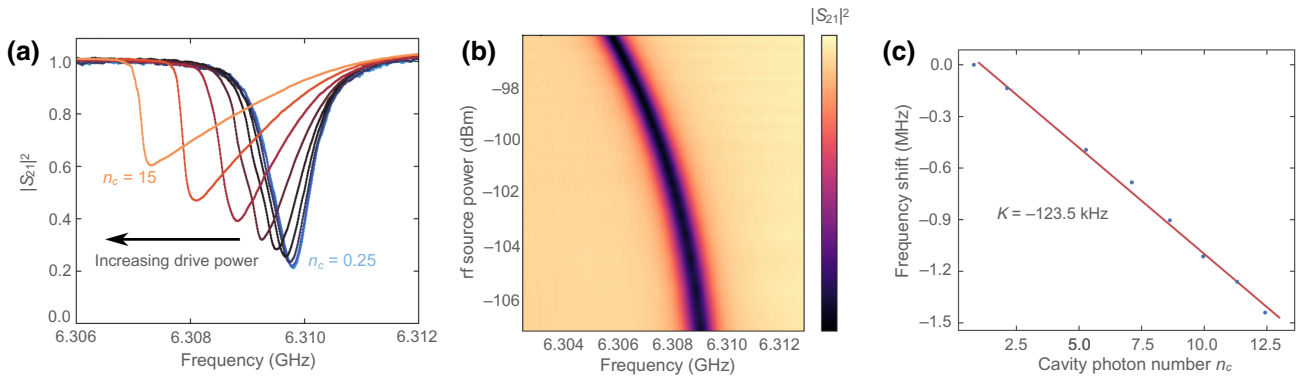


FIG. 3. Nonlinear response of a nanowire resonator. Measured nonlinear response of a nanowire resonator with resonance frequency  $f_0 = 6.3$  GHz, wire width  $w = 18 \pm 2$  nm, and wire length  $l = 460$  nm. (a) Self-Kerr response measured at increasing drive powers. The resonator shows characteristic Duffing-oscillator-type behavior. The intracavity photon number is swept from 0.25 to 15, with equal steps on a log scale. (b) Two-tone spectroscopy in the few-photon regime. A radio-frequency drive (blue-detuned by 5.3 MHz from the resonance) is used to drive the resonator and a weak probe is used to measure the coherent response. (c) Extracted Kerr shift per photon ( $K/2\pi = 123.5$  kHz) from the two-tone spectroscopy measurement.

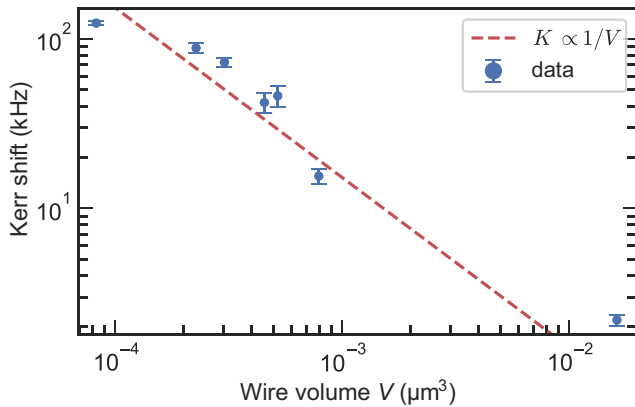


FIG. 4. Geometric dependence of nanowire nonlinearity. Measured Kerr shift for range of wire volumes varying by two orders of magnitude. The largest Kerr shift is obtained for the wire with smallest mode volume  $V = 1.2 \times 10^{-4} \mu\text{m}^3$  and decreases to 2.2 kHz for a volume of  $V = 2.3 \times 10^{-2} \mu\text{m}^3$ . The red dotted curve is a fit to the model  $K = a/V$ , with  $a = 2 \times 10^{-2} \text{ kHz } \mu\text{m}^3$ .

cavity-frequency shift, we extract the self-Kerr coefficient of each resonator [see Fig. 3(c)]. The measurement results are summarized in Table I. We find Kerr-shift-to-linewidth ( $K/\gamma$ ) ratios from 0.7% to 21%, and internal  $Q$ -factors in the range of  $0.2\text{--}3.5 \times 10^4$  (Table I). The measured self-Kerr shift is largest for the wire with smallest mode volume  $V = 1.2 \times 10^{-4} \mu\text{m}^3$ . After that, we observe a monotonic decrease in Kerr shift for increasing wire volume, in agreement with the expected  $1/V$  scaling behavior (see Fig. 4). Using a fit to the model [Eq. (4)], we extract participation ratios  $\alpha$  in the range of 0.7–0.97. These participation ratios are larger than those expected using our measured value of sheet inductance ( $L_s$ ) and the wire dimensions obtained from imaging the devices. We attribute this discrepancy to contributions to the nonlinear response from the current distribution in the capacitor pads, which are not included in our lumped-element model.

We find the internal  $Q$ -factors of the nanowires resonators to be smaller (by about an order of magnitude) than those found in lumped-element test resonators used for film characterization. Importantly, we do not observe significant wire-width dependence for the internal  $Q$ -factor; the device with the largest nonlinearity and narrowest wire width has an internal  $Q$ -factor of  $1.08 \times 10^4$ . We have verified that the measured  $Q$ -factors are dominated by energy loss, despite the presence of a slow dephasing mechanism (see Appendix E). Below, we discuss the dominant loss mechanisms in our devices and potential avenues for improving the  $K/\gamma$  ratio.

## V. DISSIPATION MECHANISMS

The narrow-gap capacitor geometry and the resulting large electric fields in our designs make our devices sensitive to TLS loss at interfaces [40,41]. Common techniques

for extracting the TLS-induced loss involve saturating the TLS bath via a coherent external drive or by elevating the measurement temperature. However, in our current experiment the small bistability threshold set by the strongly nonlinear response of the cavities does not allow for directly applying these techniques. Additionally, while these measurements are, in principle, possible in test structures with identical electric field distributions but with a diluted nonlinearity (e.g., via wider wires), the inevitable reduction in KI leads to much higher resonance frequencies beyond our setup's measurement band. Beyond TLS loss, we expect two primary sources of dissipation in our devices. The large KI fraction of the nanowire resonators makes them susceptible to dissipation from excess quasiparticles generated by stray radiation [16,42–44]. In addition, the large size of the capacitor pads, together with a small gap, results in a large effective dipole, making the resonators susceptible to radiative loss. Here, we provide order-of-magnitude estimates for loss contributions from these sources.

The rate of dissipation due to a nonequilibrium quasiparticle density  $n_{\text{qp}}$  can be predicted from the Mattis-Bardeen equations for the complex conductivity, and is given by [45]

$$\Gamma_{\text{qp}} = \frac{\alpha\omega_0}{\pi} \sqrt{\frac{2\Delta_0}{\hbar\omega_0 D(E_F)\Delta_0}} \frac{n_{\text{qp}}}{n_{\text{qp}}} \quad (6)$$

where  $\alpha$  is the KI fraction,  $\omega_0$  is the resonance frequency,  $n_{\text{qp}}$  is the excess quasiparticle density, and  $D(E_F)$  is the density of Cooper pairs at Fermi energy. We evaluate Eq. (6) using parameters reported in literature for TiN thin films [ $D(E_F) = 2 \times 10^{10} \mu\text{m}^{-3} \text{ eV}^{-1}$  [46],  $n_{\text{qp}} = 10/\mu\text{m}^3$  [44,45]], our measured critical temperature, and the simulated KI fraction  $\alpha$ . As a verification of the calculation, we find the quasiparticle-limited  $Q$ -factors of the test resonators used for film characterization (in Sec. III,  $4.8 \times 10^5$ ), in close agreement with measured  $Q$ -factors at high powers ( $2.1 \times 10^5$ ). For the nanowire resonators, the calculation gives a similar decay rate in the range of 12–14 kHz, which is much smaller than the observed values in the experiment. Interestingly, the calculated quasiparticle-limited decay rates are about an order of magnitude smaller than the largest measured single-photon Kerr shifts, pointing to the intrinsically low-loss nature of KI as a source of nonlinearity.

We estimate radiation loss contributions by modeling the near-field coupling of the nanowire resonators to the packaging box modes. Our device is packaged within a copper box with air gaps below and above the chip, with the lowest-order resonant mode located near  $f_b = 17$  GHz. We use conservative  $Q$ -factors for the microwave package mode ( $\kappa/2\pi = 35$  MHz) [47] and use analytical expressions for the electric field of coplanar capacitor plates to estimate an upper bound for radiative loss rate of  $\Gamma/2\pi \approx 60$  kHz (see Appendix F). While significant, this

source of loss does not adequately account for the observed linewidths. Ruling out quasiparticle dissipation and radiative loss, we suspect the device performance is currently limited by TLS loss.

## VI. CONCLUSION

In conclusion, we have investigated the limits of KI Kerr nonlinearity by optimizing the geometry of resonators fabricated from thin-film TiN. Confining current density in miniaturized nanowires, we have observed a nonlinearity-to-loss ratio of  $K/\gamma = 0.21 \pm 0.02$ . While the ratio achieved is not sufficient to make a qubit based on this concept in the microwave frequency band, the quadratic scaling of nonlinearity with frequency [Eq. (2)] promises future opportunities. At a frequency of 100 GHz, this scaling translates to Kerr-shift coefficients in the range of 20–30 MHz per photon. Intrinsic quality factors as large as  $3 \times 10^4$  ( $\gamma/2\pi = 3$  MHz) have previously been demonstrated using NbN films at this frequency [1]. Achieving our scaled Kerr-shift coefficients in devices with comparable quality factors would translate to the observation of a strong quantum nonlinear response. While quasiparticle-limited  $Q$ -factors of  $10^5$  are possible at low operating temperatures with our TiN film (see Appendix G), future studies of loss mechanisms in TiN, and a broader set of disordered superconductors in the millimeter-wave band are necessary. Additionally, the improved Kerr coefficients in our devices may be exploited for frequency conversion from microwave to millimeter-wave frequencies, where operation with lower pump powers and stronger nonlinearities can reduce absorption heating. Using the measured and scaled Kerr shifts at microwave and millimeter-wave frequencies, we estimate a cross-Kerr shift of  $K_{uw,mm} = 2(K_{uw}K_{mm})^{1/2} \approx 2\pi \times 3$  MHz [48]. Finally, we note the possibility of further improvements by going beyond planar geometries by using parallel-plate capacitors, where large quality factors ( $10^5$ ) have previously been demonstrated [49].

## ACKNOWLEDGMENTS

This work was supported by startup funds from the Caltech EAS division, a Braun trust grant, and the National Science Foundation (Grant No. 1733907). C.J. gratefully acknowledges support from the IQIM/AWS Postdoctoral Fellowship. We acknowledge Niv Drucker from Quantum Machines for software support while performing the cavity ringdown measurements.

## APPENDIX A: FILM CHARACTERIZATION: SHEET INDUCTANCE

We estimate the sheet inductance of the TiN thin films by fitting the extracted resonance frequency of the quarter-wave resonators with wire width  $w = 2 \mu\text{m}$  and

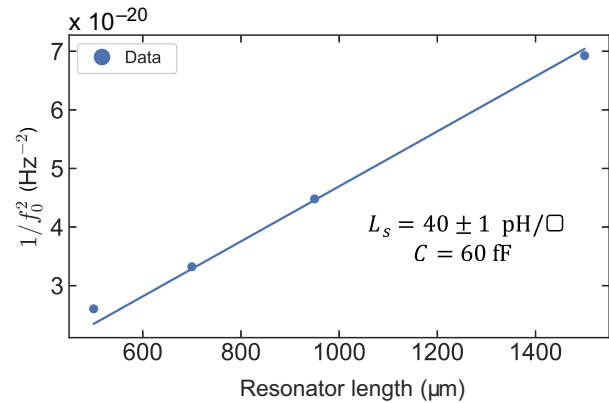


FIG. 5. Calibration of sheet inductance. Measured  $1/f_0^2$  versus wire length for quarter-wave resonators with wire width  $w = 2 \mu\text{m}$ . From the slope of the fit  $m = 4\pi^2 L_s C/w$  and capacitance extracted from simulations ( $C = 60 \text{ fF}$ ), we extract a sheet kinetic inductance of  $L_s = 40 \pm 1 \text{ pH}/\square$ .

varying wire lengths (Fig. 5). A capacitance of  $C = 60 \text{ fF}$  was extracted for the quarter-wave resonator geometry [Fig. 2(a)] using FEM simulations. From the slope  $m = 4\pi^2 L_s C/w$  of the fit shown in Fig. 5, we obtain a sheet inductance of  $L_s = 40 \pm 1 \text{ pH}/\square$ .

## APPENDIX B: FABRICATION METHODS

The TiN samples used in our experiment were deposited using reactive sputtering on a high-resistivity ( $\rho > 10 \text{ k}\Omega$ ) Si substrate and measured with an ellipsometer to have a thickness of 14 nm. Following sputtering, the wafer is diced into  $1 \times 1 \text{ cm}^2$  dies. The dies are cleaned using standard organic solvents, followed by additional cleaning using an  $\text{O}_2$  plasma etcher. Following cleaning, the chips are baked for dehydration at  $180^\circ\text{C}$  for 3 min. We then deposit ZEP 520A on the dies. The dies are postbaked at  $180^\circ\text{C}$  for 3 min. The devices are patterned using e-beam lithography (Raith EBPG 5000+, 1 nA current). The resist is developed using n-amyl acetate (ZED-N50) followed by rinsing with methyl isobutyl ketone. De-scum is performed using  $\text{O}_2$  plasma, followed by ICP-RIE using  $\text{SF}_6$  and Argon chemistry [50]. Postetching, the chips are left in N-methyl-2-pyrrolidone at  $150^\circ\text{C}$  for 2 h for ZEP removal, followed by cleaning with organic solvents and  $\text{O}_2$  plasma.

Achieving reproducible nanowire widths across fabrication runs was challenging due to variations caused by a combination of factors including temperature variations during the resist development, changes in the chemistry of the dry etch process and changes to the electron beam parameters during lithography. These factors can cause a 10–15 nm variation in the wire widths across runs. We attempted to minimize fabrication disorder by ensuring consistency of proximity error correction for dose assignment during lithography, using a consistent beam spot size

TABLE II. Line attenuation calibration.

$f$ (GHz)	Net transmission ( $S_{10}$ , dB)	Gain ( $G_C$ , dB)	Attenuation ( $A_{IN}$ , dB)
4.4	-5.5	$68.3 \pm 0.7$	$73.8 \pm 0.7$
6.30	-11.50	$64.6 \pm 0.4$	$76.1 \pm 0.4$
6.56	-11.95	$64.5 \pm 0.7$	$76.5 \pm 0.7$
7.03	-13.95	$63.6 \pm 0.9$	$77.6 \pm 0.9$
7.70	-16.90	$62.9 \pm 0.6$	$79.8 \pm 0.6$
8.07	-18.30	$61.4 \pm 0.6$	$79.7 \pm 0.6$

and by performing an extended etch chamber conditioning run to eliminate contamination before the dry etch process. After controlling for the lithography and etch steps to the extent possible, we found a 3–4 nm variation in the wire width. Controlling for developer temperature can also potentially improve the repeatability of our fabrication process [51].

### APPENDIX C: LINE ATTENUATION CALIBRATION

To calculate accurately the power delivered to the chip, we calibrate the frequency-dependent attenuation of our input line using thermometry. The input line contains cryogenic attenuation at each stage of the cryostat to minimize thermal noise conducted from room-temperature electronics to the cold stages via the input lines (see Fig. 8 for a schematic of our measurement setup) [52]. In addition, the input line consists of a cryogenic circulator (Low Noise Factory, LNF-CIC4\_12A) and a fanout switch. The output line consists of a high electron mobility transistor (HEMT) amplifier (LNF-LNC4\_8C) thermalized to the 4 K stage and a room-temperature amplifier. We first measure the overall frequency-dependent transmission of the input and output line using an rf tone sent from a signal generator. We then calibrate the total gain of the output line using thermometry. A  $50\ \Omega$  cryogenic terminator is thermalized to the mixing (MXC) stage of the cryostat. The MXC stage temperature is raised by reducing cooling power by turning off the turbo to reduce  $^3\text{He}/^4\text{He}$  mixture flow, and applying heat using the MXC stage heater. With no external input

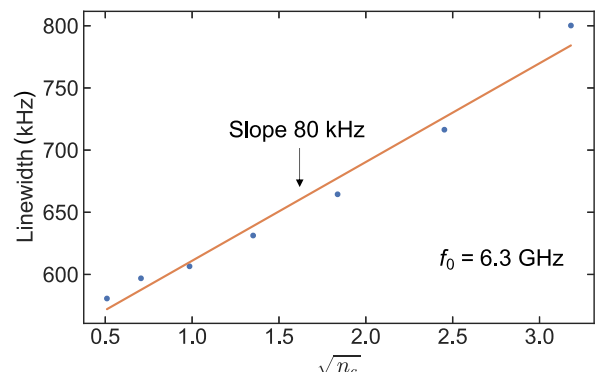


FIG. 6. Shot-noise-induced dephasing in self-Kerr response. Measured cavity linewidth versus photon number for the self-Kerr data shown in Fig. 3(a). The increase in linewidth can be attributed to dephasing due to shot noise in the cavity photon number when the cavity is resonantly driven.

power, we measure the output power from the amplifier chain with a spectrum analyzer at different mixing stage temperatures  $T_{\text{MXC}}$ . The measured output has contributions from the thermal noise of the resistor at the MXC stage, and the HEMT noise characterized by a fixed noise temperature  $T_{\text{HEMT}}$ . The output power measured in an IF bandwidth  $\Delta\nu_{\text{IF}}$  on the spectrum analyzer is equal to the sum of the Johnson-Nyquist noise from the two sources and is given by

$$P_{\text{OUT}} = \Delta\nu_{\text{IF}} k_B G_C (T_{\text{MXC}} + T_{\text{HEMT}}). \quad (\text{C1})$$

Here,  $G_C$  is the net absolute gain factor of the output line from the chip. At  $T_{\text{MXC}} = 10\ \text{mK}$ , the measured output power is dominated by HEMT noise. The output gain  $G_C$  can then be calculated by subtracting the contribution of the HEMT noise from the total output power measured at various  $T_{\text{MXC}}$ . We perform this measurement at four different MXC temperatures between  $730\ \text{mK}$  and  $1.05\ \text{K}$ . The mean and standard deviation of the four measurements are used to obtain  $G_C$ . We use a factor  $\eta = (hv/kT)/(\exp(hv/kT) - 1)$  to account for corrections to Eq. (C1) due to the Bose-Einstein distribution in the regime  $h\nu \sim k_B T$  [53]. The input line attenuation can be

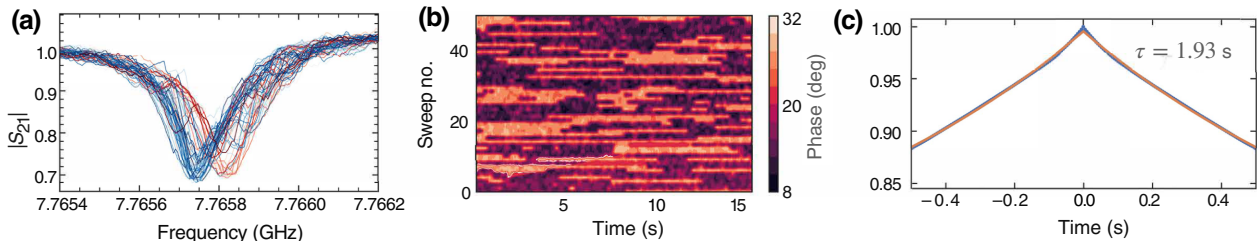


FIG. 7. Telegraph noise. (a) Single-shot measurements of the frequency response of the resonator with the narrowest linewidth ( $f_0 = 7.7\ \text{GHz}$ ). The resonator exhibits switching between two states. (b) Measured time-dependent phase response, showing characteristics of a telegraph process. (c) Auto-correlation of the time-dependent phase of the resonator. We extract a switching time of  $\tau = 1.93\ \text{s}$ .

calculated using

$$A_{\text{IN}}[\text{dB}] + G_C[\text{dB}] = S_{\text{IO}}[\text{dB}]. \quad (\text{C2})$$

Here,  $S_{\text{IO}}$  is the net transmission of the input-output lines measured at different frequencies and  $G_C[\text{dB}]$  is the calibrated output gain in dB. This net transmission is measured at  $T_{\text{MXC}} = 10 \text{ mK}$ . The results are summarized in Table II. In this calibration, as the temperature of the entire MXC stage is increased during the measurement, any additional loss in the microwave components in the *output* lines thermalized to the MXC stage results in injection of thermal noise at  $T_{\text{MXC}}$ , making Eq. (C1) accurate for the gain calibration. We note that any additional attenuation at 1 K in the *input* lines does not affect the gain calibration. Our calibration does not account for the small loss due to the microwave components in the output line which are thermalized to the mixing stage. These include two passes through the circulators LNF-CIC4\_12A (0.2 dB insertion loss per pass) and 18 inches of microwave cables (micro-coax,  $\alpha = 0.4 \text{ dB/m}$  [54]). This results in an uncertainty of 0.6 dB in the calibrated line attenuation, which has been included in error bars reported in Table II.

#### APPENDIX D: SHOT-NOISE-INDUCED DEPHASING

The measured self-Kerr response of the nanowire resonators shows an increased linewidth when the cavity is populated with few photons [Fig. 3(a)]. The relatively large ratios of Kerr shift to linewidth create the possibility of dephasing due to shot noise when the cavity is populated via a resonant drive. As shown in Fig. 6, the measured linewidth increases in proportion to  $\sqrt{n_c}K$ . Additionally, we extract a slope of 80 kHz for this linear dependence, which is close to the measured self-Kerr coefficient for this resonator (123.5 kHz). In contrast, we do not observe a significant linewidth broadening in the two-tone spectroscopy measurement, where the cavity is driven off-resonantly [Fig. 3(b)]. In this case, the cavity is only virtually populated, and we estimate the increase in linewidth to be proportional to  $nK^2/\Delta$ , which is of the order of 10 kHz [39].

#### APPENDIX E: TELEGRAPH NOISE AND $T_1$ LIFETIME MEASUREMENT

We observe telegraph noise in the frequency response of the resonator with the narrowest linewidth (device No. 7, see Table I). We perform single-shot VNA measurements to capture the fast dephasing of this resonator. The resonator exhibits switching between two states, as shown in Fig. 7(a). To measure the characteristic transition time  $\tau$  between the two states, we measure the phase response of the resonator continuously using the zero-span mode of the

VNA. As shown in Fig. 7(b), the phase response is reminiscent of the telegraph process. The switching time can be extracted from the autocorrelation function of the telegraph process, given by  $\langle \phi(t)\phi(t') \rangle \propto \exp -2|t-t'|/\tau$ , where  $\phi(t)$  is the time-dependent phase shown in Fig. 7(b). We extract a switching time of  $\tau = 1.93 \text{ s}$ .

We perform cavity ringdown spectroscopy on this resonator to extract its  $T_1$  lifetime. The resonator was driven

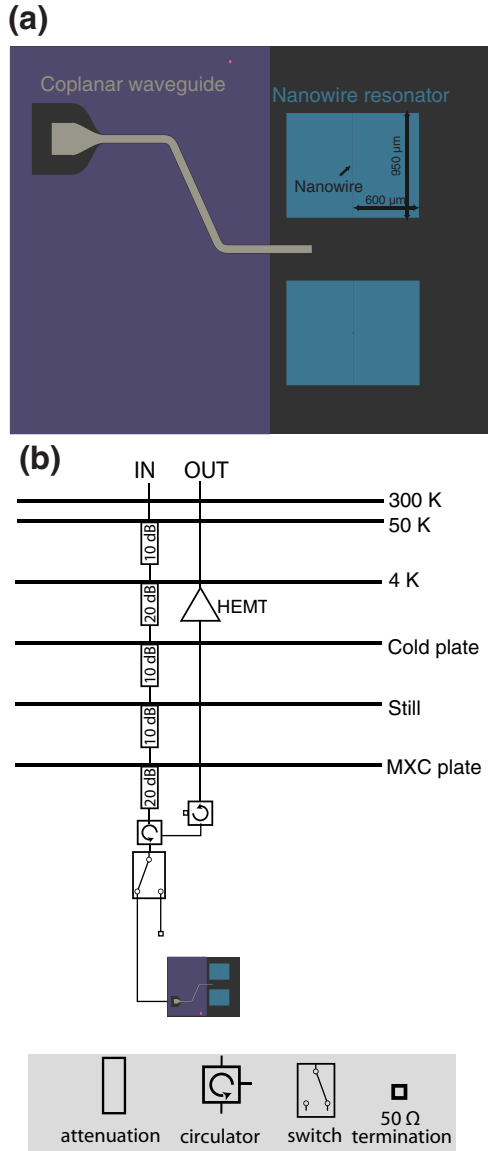


FIG. 8. Measurement setup. (a) The nanowire resonators are capacitively coupled to a coplanar waveguide used for drive and readout. (b) Measurement setup within the dilution fridge. The input line IN contains a total of 70 dB attenuation to reduce thermal noise from room-temperature electronics. Measurements are performed in reflection using a circulator. The output line consists of a high electron mobility transistor amplifier thermalized to the 4 K stage and additional room-temperature amplifiers (not shown).

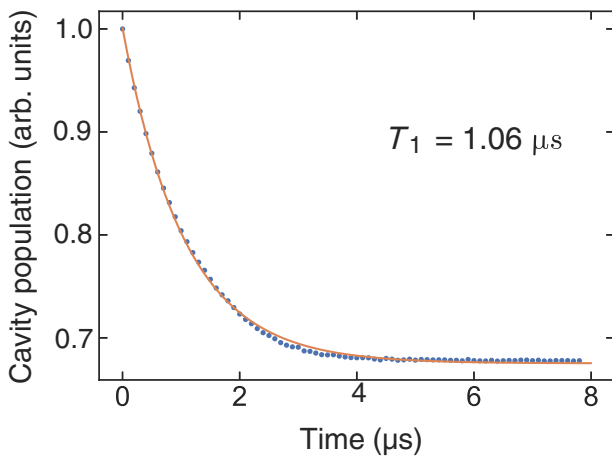


FIG. 9. Cavity-ring down spectroscopy. Time-dependent energy decay of the resonator after turning off the drive pulse. We measure a  $T_1$  lifetime of  $1.06 \mu\text{s}$ , corresponding to an instantaneous linewidth of  $150 \text{ kHz}$  for the  $7.7 \text{ GHz}$  resonator.

using a modulated signal generated from a field programmable gate array, up-converted by frequency mixing with an rf signal generator acting as the local oscillator. The resonator is driven using a  $5 \mu\text{s}$  pulse, sufficiently long to ensure that the cavity population is saturated. The drive is then turned off abruptly. The drive power was set to be sufficiently low such that the resonator response is in the linear regime. The time-dependent decay of the cavity population is shown in Fig. 9. The measured  $T_1$  lifetime is  $1.06 \mu\text{s}$ , corresponding to a decay rate of  $150 \text{ kHz}$ . Comparing this value with the measured resonator linewidth with long averages ( $220 \text{ kHz}$ ) bounds the contributions from dephasing to approximately  $70 \text{ kHz}$ .

Telegraph noise has been previously observed in KI resonators [55–58]. Potential mechanisms for the origin of this noise are strong coupling to TLS [55,57,58] or quasi-particle burst noise from high-energy particles [56], and

requires further investigation which is beyond the scope of this study.

## APPENDIX F: RADIATION LOSS CALCULATION

We estimate the radiation loss of the resonator to the box using the Purcell decay expression in the far-detuned regime, where the resonator decay rate can be estimated as

$$\Gamma = \frac{\kappa g^2}{\Delta^2}. \quad (\text{F1})$$

Here, we assume  $\Delta \gg \kappa, g$ . The parameter  $\Delta/2\pi = f_b - f_0$  is the detuning between the resonator and the box mode  $f_b$  and  $\kappa/2\pi = f_b/Q$  is the decay rate of the box mode. The coupling rate  $g$  between the resonator and the box mode is related to the electric field overlap between the cavity and the box modes, and is given by [59,60]

$$\hbar g = \sqrt{\frac{\hbar\omega_r}{2\epsilon_0 V_r}} \sqrt{\frac{\hbar\omega_b}{2\epsilon_0 V_b}} \int dV \epsilon \epsilon_0 |\mathbf{a}_r^* \cdot \mathbf{a}_b|, \quad (\text{F2})$$

where  $V_r$  and  $V_b$  are the effective mode volumes of the resonator and box mode, respectively. The coefficients  $\mathbf{a}_r$  and  $\mathbf{a}_b$  are normalized, dimensionless amplitudes such that the electric-field of  $\mathbf{E}_i$  is given by  $\mathbf{E}_i = \sqrt{\hbar\omega_i/2\epsilon_0 V_i} \mathbf{a}_i$ ,  $i \in [r, b]$ . The integral is carried over the volume of the box. The field distribution  $\mathbf{E}_r$  of the resonator mode can be approximated from analytical expressions for coplanar capacitor pads obtained using conformal mapping [61,62]. The electric field distribution for the resonator mode is shown in Fig. 10. As expected, the field distribution resembles that of a dipole due to the large electric field in the small capacitor gap. Using FEM simulations, the lowest-order box mode is found to be a  $\text{TE}_{011}$  mode at  $f_b = 17 \text{ GHz}$ . Assuming the resonator is placed in the center of the box where the E-field of the box mode peaks, we evaluate Eq. (F2) numerically and determine a coupling rate

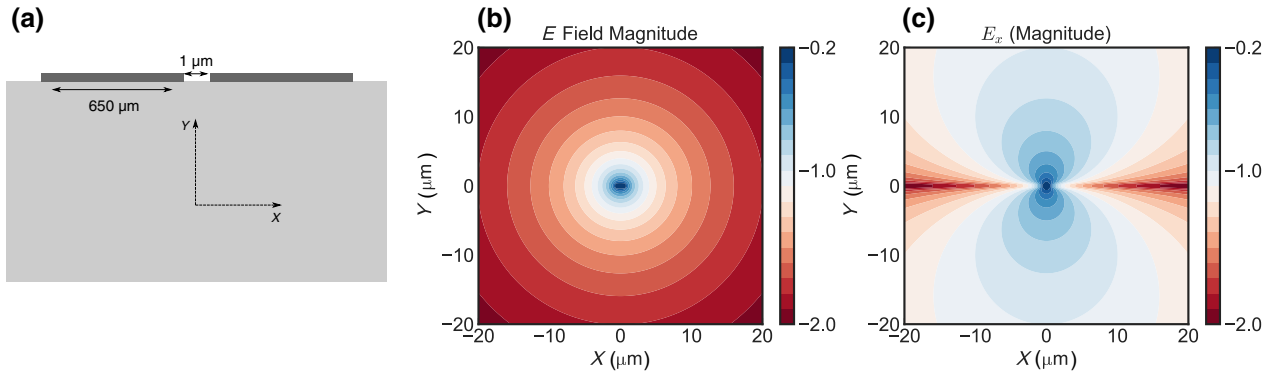


FIG. 10. E-field distribution of coplanar capacitor pads. (a) Cross section of the coplanar capacitor pads. (b) E-field magnitude of coplanar capacitor pads in the vicinity of the capacitor gap, calculated from analytical expressions using conformal mapping. The field distribution resembles that of a dipole. (c) In-plane ( $E_x$ ) field magnitude, which results in the dominant coupling to the  $\text{TE}_{011}$  box mode.

$g/2\pi = 410$  MHz. For a typical resonator frequency  $f = 7$  GHz and assuming a typical package mode  $Q \approx 500$ , we obtain a radiation loss rate of  $\Gamma/2\pi = 57$  kHz using Eq. (F1). The degenerate TE<sub>101</sub> mode does not couple to the resonator mode due to its orthogonal polarization. The immediate higher-order modes at higher frequencies also do not contribute significantly as they have E-field nodes at the center of the box, and the decay rate is further suppressed due to their large detuning  $\Delta$  relative to the resonator mode.

## APPENDIX G: FREQUENCY DEPENDENCE OF QUASIPARTICLE LOSS

Figure 11 shows the calculated values for the quasiparticle-limited  $Q$ -factors based on the surface impedance from Mattis-Bardeen theory, as a function of operating temperature and frequency [10,35,37,63]. At low operating temperatures  $T$  such that  $T_c/T > 6$ , the quasiparticle-limited loss has a weak dependence on frequency. At higher operating temperatures, the quasiparticle loss becomes a stronger function of operating frequency.

For the film used in this work, we measure a  $T_c = 2.9$  K, corresponding to  $\Delta_0/h = 110$  GHz. As evident in Fig. 11, at operating temperatures  $T$  between 10 mK and 500 mK ( $T_c/T \approx 6$ ), the quasiparticle-limited  $Q$ -factors are about  $10^5$  and we do not expect to see significant degradation of the  $Q$ -factors in the frequency range up to 110 GHz. However, operating at elevated temperatures (above 500 mK,  $T_c/T < 6$ ) makes the quasiparticle-limited quality factors a stronger function of the frequency and is expected to cause a reduction in  $Q$ -factor by a factor of 2–5 in this frequency range (see Fig. 11).

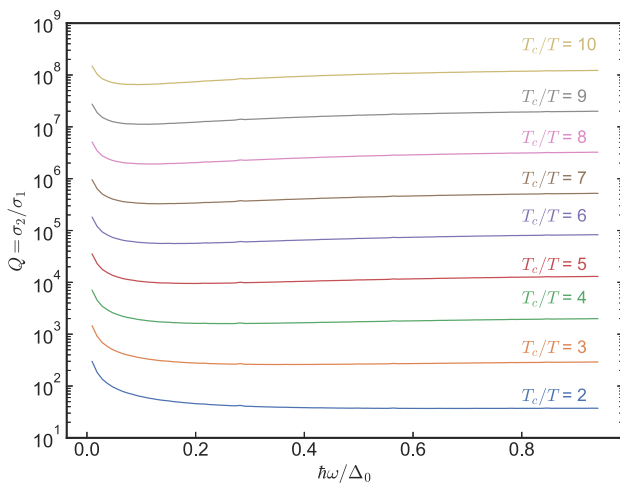


FIG. 11. Quasiparticle-limited  $Q$ -factors. Calculated quasiparticle-limited  $Q$ -factors based on the surface impedance obtained from Mattis-Bardeen theory as a function of operating temperature and frequency.

- [1] A. Anferov, A. Suleymanzade, A. Oriani, J. Simon, and D. I. Schuster, Millimeter-Wave Four-Wave Mixing via Kinetic Inductance for Quantum Devices, *Phys. Rev. Appl.* **13**, 024056 (2020).
- [2] M. Pechal and A. H. Safavi-Naeini, Millimeter-wave interconnects for microwave-frequency quantum machines, *Phys. Rev. A* **96**, 042305 (2017).
- [3] A. Lingenfelter, D. Roberts, and A. A. Clerk, Unconditional Fock state generation using arbitrarily weak photonic nonlinearities, *Sci. Adv.* **7**, eabj1916 (2021).
- [4] A. Imamoglu, H. Schmidt, G. Woods, and M. Deutsch, Strongly Interacting Photons in a Nonlinear Cavity, *Phys. Rev. Lett.* **79**, 1467 (1996).
- [5] F. Faramarzi, P. Day, J. Glasby, S. Sykpkens, M. Colangelo, R. Chamberlin, M. Mirhosseini, K. Schmidt, K. K. Berggren, and P. Mauskopf, Initial design of a W-band superconducting kinetic inductance qubit, *IEEE Trans. Appl. Supercond.* **31**, 1 (2021).
- [6] P. Winkel, K. Borisov, L. Grünhaupt, D. Rieger, M. Spiecker, F. Valenti, A. V. Ustinov, W. Wernsdorfer, and I. M. Pop, Implementation of a Transmon Qubit Using Superconducting Granular Aluminum, *Phys. Rev. X* **10**, 031032 (2020).
- [7] Y. Schön, J. N. Voss, M. Wildermuth, A. Schneider, S. T. Skacel, M. P. Weides, J. H. Cole, H. Rotzinger, and A. V. Ustinov, Rabi oscillations in a superconducting nanowire circuit, *npj Quantum Mater.* **5**, 1 (2020).
- [8] N. Maleeva, L. Grünhaupt, T. Klein, F. Levy-Bertrand, O. Dupre, M. Calvo, F. Valenti, P. Winkel, F. Friedrich, W. Wernsdorfer, A. V. Ustinov, H. Rotzinger, A. Monfardini, M. V. Fistul, and I. M. Pop, Circuit quantum electrodynamics of granular aluminum resonators, *Nat. Commun.* **9**, 3889 (2018).
- [9] N. A. Masluk, I. M. Pop, A. Kamal, Z. K. Minev, and M. H. Devoret, Microwave Characterization of Josephson Junction Arrays: Implementing a Low Loss Superinductance, *Phys. Rev. Lett.* **109**, 137002 (2012).
- [10] J. Zmuidzinas, Superconducting microresonators: Physics and applications, *Annu. Rev. Condens. Matter Phys.* **3**, 169 (2012).
- [11] H. G. Leduc, B. Bumble, P. K. Day, B. H. Eom, J. Gao, S. Golwala, B. A. Mazin, S. McHugh, A. Merrill, D. C. Moore, O. Noroozian, A. D. Turner, and J. Zmuidzinas, Titanium nitride films for ultrasensitive microresonator detectors, *Appl. Phys. Lett.* **97**, 102509 (2010).
- [12] M. R. Vissers, J. Gao, D. S. Wisbey, D. A. Hite, C. C. Tsuei, A. D. Corcoles, M. Steffen, and D. P. Pappas, Low loss superconducting titanium nitride coplanar waveguide resonators, *Appl. Phys. Lett.* **97**, 232509 (2010).
- [13] P. C. J. J. Coumou, M. R. Zuiddam, E. F. C. Driessen, P. J. de Visser, J. J. A. Baselmans, and T. M. Klapwijk, Microwave properties of superconducting atomic-layer deposited TiN films, *IEEE Trans. Appl. Supercond.* **23**, 7500404 (2013).
- [14] J. M. Sage, V. Bolkhovsky, W. D. Oliver, B. Turek, and P. B. Welander, Study of loss in superconducting coplanar waveguide resonators, *J. Appl. Phys.* **109**, 063915 (2011).
- [15] D. Niepce, J. Burnett, and J. Bylander, High Kinetic Inductance NbN Nanowire Superconductors, *Phys. Rev. Appl.* **11**, 044014 (2019).

- [16] L. Grünhaupt, M. Spiecker, D. Gusekova, N. Maleeva, S. T. Skacel, I. Takmakov, F. Valenti, P. Winkel, H. Rotzinger, W. Wernsdorfer, A. V. Ustinov, and I. M. Pop, Granular aluminum as a superconducting material for high-impedance quantum circuits, *Nat. Mater.* **18**, 816 (2019).
- [17] P. Kamenov, W.-S. Lu, K. Kalashnikov, T. DiNapoli, M. T. Bell, and M. E. Gershenson, Granular Aluminum Meandered Superinductors for Quantum Circuits, *Phys. Rev. Appl.* **13**, 054051 (2020).
- [18] A. J. Landig, J. V. Koski, P. Scarlino, U. C. Mendes, A. Blais, C. Reichl, W. Wegscheider, A. Wallraff, K. Ensslin, and T. Ihn, Coherent spin–photon coupling using a resonant exchange qubit, *Nature* **560**, 179 (2018).
- [19] N. Samkharadze, A. Bruno, P. Scarlino, G. Zheng, D. P. DiVincenzo, L. DiCarlo, and L. M. K. Vandersypen, High-Kinetic-Inductance Superconducting Nanowire Resonators for Circuit QED in a Magnetic Field, *Phys. Rev. Appl.* **5**, 044004 (2016).
- [20] B. Ho Eom, P. K. Day, H. G. LeDuc, and J. Zmuidzinas, A wideband, low-noise superconducting amplifier with high dynamic range, *Nat. Phys.* **8**, 623 (2012).
- [21] L. J. Swenson, P. K. Day, B. H. Eom, H. G. Leduc, N. Llobart, C. M. McKenney, O. Noroozian, and J. Zmuidzinas, Operation of a titanium nitride superconducting microresonator detector in the nonlinear regime, *J. Appl. Phys.* **113**, 104501 (2013).
- [22] J. Zmuidzinas and P. L. Richards, Superconducting detectors and mixers for millimeter and submillimeter astrophysics, *Proc. IEEE* **92**, 1597 (2004).
- [23] M. Malnou, M. Vissers, J. Wheeler, J. Aumentado, J. Hubmayr, J. Ullom, and J. Gao, Three-Wave Mixing Kinetic Inductance Traveling-Wave Amplifier with Near-Quantum-Limited Noise Performance, *PRX Quantum* **2**, 010302 (2021).
- [24] S. P. Chockalingam, M. Chand, J. Jesudasan, V. Tripathi, and P. Raychaudhuri, Superconducting properties and Hall effect of epitaxial NbN thin films, *Phys. Rev. B* **77**, 214503 (2008).
- [25] M. Xu, R. Cheng, Y. Wu, G. Liu, and H. X. Tang, Magnetic field-resilient quantum-limited parametric amplifier, [arXiv:2209.13652 \[quant-ph\]](https://arxiv.org/abs/2209.13652) (2022).
- [26] M. Xu, X. Han, W. Fu, C.-L. Zou, and H. X. Tang, Frequency-tunable high- $Q$  superconducting resonators via wireless control of nonlinear kinetic inductance, *Appl. Phys. Lett.* **114**, 192601 (2019).
- [27] A. Bozkurt, H. Zhao, C. Joshi, H. G. LeDuc, P. K. Day, and M. Mirhosseini, A quantum electromechanical interface for long-lived phonons, [arXiv:2207.10972 \[quant-ph\]](https://arxiv.org/abs/2207.10972) (2022).
- [28] P. C. J. J. Coumou, Electrodynamics of Strongly Disordered Superconductors, Ph.D. thesis, TU Delft (2015).
- [29] B. Sacépé, C. Chapelier, T. I. Baturina, V. M. Vinokur, M. R. Baklanov, and M. Sanquer, Disorder-Induced Inhomogeneities of the Superconducting State Close to the Superconductor-Insulator Transition, *Phys. Rev. Lett.* **101**, 157006 (2008).
- [30] U. S. Pracht, N. Bachar, L. Benfatto, G. Deutscher, E. Farber, M. Dressel, and M. Scheffler, Enhanced Cooper pairing versus suppressed phase coherence shaping the superconducting dome in coupled aluminum nanograins, *Phys. Rev. B* **93**, 100503 (2016).
- [31] A. S. Kher, Superconducting Nonlinear Kinetic Inductance Devices, Ph.D. thesis, California Institute of Technology (2017).
- [32] A. Anthore, H. Pothier, and D. Esteve, Density of States in a Superconductor Carrying a Supercurrent, *Phys. Rev. Lett.* **90**, 127001 (2003).
- [33] S. Rasmussen, K. Christensen, S. Pedersen, L. Kristensen, T. Bækkegaard, N. Loft, and N. Zinner, Superconducting Circuit Companion—An Introduction with Worked Examples, *PRX Quantum* **2**, 040204 (2021).
- [34] A. Shearow, G. Koolstra, S. J. Whiteley, N. Earnest, P. S. Barry, F. J. Heremans, D. D. Awschalom, E. Shirokoff, and D. I. Schuster, Atomic layer deposition of titanium nitride for quantum circuits, *Appl. Phys. Lett.* **113**, 212601 (2018).
- [35] J. Gao, The physics of superconducting microwave resonators, Ph.D. Thesis, California Institute of Technology (2008).
- [36] G. Klemencic, Microwave and superconducting techniques for measurements on unconventional Josephson junctions, PhD Thesis, University of Birmingham (2013).
- [37] J. Garrett, Electrical properties of superconductors using mattis-bardeen theory, GitHub repository (2021).
- [38] C. Eichler, C. Lang, J. M. Fink, J. Govenius, S. Filipp, and A. Wallraff, Observation of Entanglement between Itinerant Microwave Photons and a Superconducting Qubit, *Phys. Rev. Lett.* **109**, 240501 (2012).
- [39] J. Gambetta, A. Blais, D. I. Schuster, A. Wallraff, L. Frunzio, J. Majer, M. H. Devoret, S. M. Girvin, and R. J. Schoelkopf, Qubit-photon interactions in a cavity: Measurement-induced dephasing and number splitting, *Phys. Rev. A* **74**, 042318 (2006).
- [40] A. Melville, G. Calusine, W. Woods, K. Serniak, E. Golden, B. M. Niedzielski, D. K. Kim, A. Sevi, J. L. Yoder, E. A. Dauler, and W. D. Oliver, Comparison of dielectric loss in titanium nitride and aluminum superconducting resonators, *Appl. Phys. Lett.* **117**, 124004 (2020).
- [41] K. R. Amin, C. Ladner, G. Jourdan, S. Hentz, N. Roch, and J. Renard, Loss mechanisms in TiN high impedance superconducting microwave circuits, *Appl. Phys. Lett.* **120**, 164001 (2022).
- [42] C. R. H. McRae, H. Wang, J. Gao, M. R. Vissers, T. Brecht, A. Dunsworth, D. P. Pappas, and J. Mutus, Materials loss measurements using superconducting microwave resonators, *Rev. Sci. Instrum.* **91**, 091101 (2020).
- [43] J. M. Kreikebaum, A. Dove, W. Livingston, E. Kim, and I. Siddiqi, Optimization of infrared and magnetic shielding of superconducting TiN and Al coplanar microwave resonators, *Supercond. Sci. Technol.* **29**, 104002 (2016).
- [44] I. Siddiqi, Engineering high-coherence superconducting qubits, *Nat. Rev. Mater.* **6**, 875 (2021).
- [45] R. Barends, J. Wenner, M. Lenander, Y. Chen, R. C. Bialczak, J. Kelly, E. Lucero, P. O’Malley, M. Mariantoni, D. Sank, H. Wang, T. C. White, Y. Yin, J. Zhao, A. N. Cleland, J. M. Martinis, and J. J. A. Baselmans, Minimizing quasiparticle generation from stray infrared light in superconducting quantum circuits, *Appl. Phys. Lett.* **99**, 113507 (2011).
- [46] J. Gao, M. R. Vissers, M. O. Sandberg, F. C. S. da Silva, S. W. Nam, D. P. Pappas, D. S. Wisbey, E. C. Langman, S. R. Meeker, B. A. Mazin, H. G. Leduc, J. Zmuidzinas, and K. D. Irwin, A titanium-nitride near-infrared kinetic

- inductance photon-counting detector and its anomalous electrodynamics, *Appl. Phys. Lett.* **101**, 142602 (2012).
- [47] S. Huang, B. Lienhard, G. Calusine, A. Vepsäläinen, J. Braumüller, D. K. Kim, A. J. Melville, B. M. Niedzielski, J. L. Yoder, B. Kannan, T. P. Orlando, S. Gustavsson, and W. D. Oliver, Microwave Package Design for Superconducting Quantum Processors, *PRX Quantum* **2**, 020306 (2021).
- [48] Z. K. Minev, Z. Leghtas, S. O. Mundhada, L. Christakis, I. M. Pop, and M. H. Devoret, Energy-participation quantization of Josephson circuits, *npj Quantum Inf.* **7**, 1 (2021).
- [49] A. D. Beyer, M. I. Hollister, J. Sayers, C. F. Frez, P. K. Day, and S. R. Golwala, Fabricating with crystalline Si to improve superconducting detector performance, *J. Phys.: Conf. Ser.* **834**, 012006 (2017).
- [50] M. Sandberg, M. R. Vissers, J. S. Kline, M. Weides, J. Gao, D. S. Wisbey, and D. P. Pappas, Etch induced microwave losses in titanium nitride superconducting resonators, *Appl. Phys. Lett.* **100**, 262605 (2012).
- [51] S. Yasin, D. G. Hasko, and H. Ahmed, Comparison of MIBK/IPA and water/IPA as PMMA developers for electron beam nanolithography, *Microelectronic Engineering Micro- and Nano-Engineering* **2001**, **61–62**, 745 (2002).
- [52] S. Krinner, S. Storz, P. Kurpiers, P. Magnard, J. Heinsoo, R. Keller, J. Luetolf, C. Eichler, and A. Wallraff, Engineering cryogenic setups for 100-qubit scale superconducting circuit systems, *EPJ Quantum Technol.* **6**, 2 (2019).
- [53] H. Nyquist, Thermal agitation of electric charge in conductors, *Phys. Rev.* **32**, 110 (1928).
- [54] P. Kurpiers, T. Walter, P. Magnard, Y. Salathe, and A. Wallraff, Characterizing the attenuation of coaxial and rectangular microwave-frequency waveguides at cryogenic temperatures, *EPJ Quantum Technol.* **4**, 1 (2017).
- [55] W. Zhang, K. Kalashnikov, W.-S. Lu, P. Kamenov, T. DiNapoli, and M. E. Gershenson, Microresonators Fabricated from High-Kinetic-Inductance Aluminum Films, *Phys. Rev. Appl.* **11**, 011003 (2019).
- [56] L. Grünhaupt, N. Maleeva, S. T. Skacel, M. Calvo, F. Levy-Bertrand, A. V. Ustinov, H. Rotzinger, A. Monfardini, G. Catelani, and I. M. Pop, Loss Mechanisms and Quasiparticle Dynamics in Superconducting Microwave Resonators Made of Thin-Film Granular Aluminum, *Phys. Rev. Lett.* **121**, 117001 (2018).
- [57] D. Niepce, Superinductance and Fluctuating Two-Level Systems: Loss and Noise in Disordered and NonDisordered Superconducting Quantum Devices, Ph.D. thesis, Chalmers University of Technology (2020).
- [58] H. le Sueur, A. Svilans, N. Bourlet, A. Murani, L. Bergé, L. Dumoulin, and P. Joyez, Microscopic charged fluctuators as a limit to the coherence of disordered superconductor devices, [arXiv:1810.12801](https://arxiv.org/abs/1810.12801) [cond-mat] (2018).
- [59] Z. Lin, X. Liang, M. Lončar, S. G. Johnson, and A. W. Rodriguez, Cavity-enhanced second-harmonic generation via nonlinear-overlap optimization, *Optica* **3**, 233 (2016).
- [60] W. T. M. Irvine, K. Hennessy, and D. Bouwmeester, Strong Coupling between Single Photons in Semiconductor Microcavities, *Phys. Rev. Lett.* **96**, 057405 (2006).
- [61] Appendix K: Electric field distribution in coplanar electrodes, in *Beam Propagation Method for Design of Optical Waveguide Devices* (John Wiley & Sons, Ltd, 2015), p. 351.
- [62] O. Ramer, Integrated optic electrooptic modulator electrode analysis, *IEEE J. Quantum Electron.* **18**, 386 (1982).
- [63] P. J. De Visser, Quasiparticle Dynamics in Aluminium Superconducting Microwave Resonators, Ph.D. thesis, TU Delft (2014).